Biomedical Optics EXPRESS

A compact photonic resonator absorption microscope for point of care digital resolution nucleic acid molecular diagnostics

SHREYA GHOSH,[1,9] NANTAO LI,[1,2,9] YANYU XIONG,[1,2] YOUNG-GU JU,[3] MICHAEL P. RATHSLAG,[4] EGE G. ONAL,[4] ERIKA FALKIEWICZ,[5] MANISH KOHLI,[6] AND BRIAN T. CUNNINGHAM[1,2,4,7,8,10]

[1] *Holonyak Micro and Nanotechnology Laboratory, University of Illinois at Urbana-Champaign, Urbana, IL 61801, USA*
[2] *Department of Electrical and Computer Engineering, University of Illinois at Urbana-Champaign, Urbana, IL 61801, USA*
[3] *Department of Physics Education, Kyungpook National University, 80 Daehak-ro, Sangyeok-dong, Buk-gu, Daegu, Republic of Korea*
[4] *Department of Bioengineering, University of Illinois at Urbana-Champaign, Urbana, IL 61801, USA*
[5] *School of Integrative Biology, University of Illinois at Urbana-Champaign, Urbana, IL 61801, USA*
[6] *Huntsman Cancer Institute, University of Utah, Salt Lake City, UT 84112, USA*
[7] *Carl R. Woese Institute for Genomic Biology, University of Illinois at Urbana-Champaign, Urbana, IL 61801, USA*
[8] *Cancer Center at Illinois, University of Illinois at Urbana-Champaign, Urbana, IL 61801, USA*
[9] *S. G. and N. L. contributed equally to this work*
[10] *bcunning@illinois.edu*

Abstract: Rapid, sensitive, and selective detection of nucleic acid biomarkers for health diagnostic applications becomes feasible for point of care scenarios when the detection instrument is inexpensive, simple, and robust. Here, we report the design, implementation, and characterization of a point of care instrument for photonic resonator absorption microscopy (PRAM) that takes advantage of resonant optical coupling between plasmonic gold nanoparticle tags and a photonic crystal (PC) surface. Matching the PC resonant wavelength to the gold nanoparticle's surface plasmon wavelength generates localized and efficient quenching of the PC resonant reflection intensity, resulting in the ability to clearly detect and count individual gold nanoparticles when they are captured on the PC surface. Surface-captured nanoparticles are observed by illuminating the PC at normal incidence with polarized light from a low-intensity red LED, and recording of PC reflected intensity on an inexpensive CMOS image sensor. A contrast limited adaptive histogram equalization (CLAHE) image processing algorithm was applied to derive counts of captured nanoparticles. The instrument is utilized in the context of an activate capture + digital counting (AC + DC) assay for a specific miRNA sequence, using nucleic acid toehold probes applied to gold nano-urchin (AuNU) nanoparticles to achieve 160 aM detection limits in a 30 min. assay.

© 2021 Optical Society of America under the terms of the OSA Open Access Publishing Agreement

1. Introduction

Sensors play an essential role in the detection of molecular biomarkers such as nucleic acids and proteins for applications that include disease diagnostics, therapy effectiveness monitoring, health/wellness monitoring, and environmental analysis. While the currently dominant paradigm for non-urgent diagnostic applications is to send a sample to a laboratory facility for analysis, there is increasing interest in obtaining results immediately by performing analysis at the location where the sample is collected (referred to as the Point of Care (POC) for medical diagnostics) [1–3]. While POC analysis circumvents the need to preserve the sample during transport, it also

#427475 https://doi.org/10.1364/BOE.427475
Journal © 2021 Received 12 Apr 2021; revised 24 Jun 2021; accepted 27 Jun 2021; published 6 Jul 2021
Corrected: 12 Jul 2021

Biomedical Optics EXPRESS

demands a simple assay protocol whose result can be measured with an inexpensive, portable, compact (desktop size) and robust detection instrument. Further desirable characteristics for POC diagnostic approaches are an output that is easily quantified, large dynamic range, a simple workflow, and a rapid time to obtain a result.

Nanoparticle (NP) tagging is emerging as an effective approach for quantitative single molecule detection, due to the unique physical/chemical properties and flexibility offered by nanomaterials [4–6]. For instance, the nanometer-scale dimensions of noble metal nanoparticles, in combination with their abundance of free electrons, offers light confinement smaller than the diffraction limit and thus high sensitivity assisted by surface plasmons [7]. Nanoscale light emitters such as quantum dots and upconverting nanoparticles provide a robust luminescent platform for biosensing with excellent contrast of signal to background noise when combined with high intensity illumination and sensitive photon-counting image sensors. One of the new frontiers in single molecule biosensing is to break down the ensemble signal from the sensor/transducer into "digitized" signals that enable counting of each detected molecule [8]. When target molecules are sparsely populated on the biosensor surface, digital resolution detection approaches provide quantitative analysis of their spatial distribution and the kinetic association/dissociation with immobilized capture molecules. In order to achieve parallel monitoring over a large sensing area, widefield microscopy is often utilized for digital biosensing where nanoparticles are used as tags. A clear contrast between the target signal and the non-specific background noise is essential for providing the accuracy and reproducibility in single molecule biosensing. While label-free optical sensing by interferometric scattering [8–12], can reach the single-molecule level of sensitivity, it is accompanied by stringent requirements for controlling the environment of the detection system, such as removal of mechanical vibrations and mitigation of temperature drift. The incorporation of nanoparticles as contrast agents for digital resolution biosensing significantly reduces the complexity of the transducer in comparison to label-free techniques, as the detected signal can be orders of magnitude greater than the background noise. Taking the throughput efficiency into account, a conventional wide-field optical microscopy system is an excellent sensing platform in which both a large sensing area and single-nanoparticle resolution can be achieved.

Photonic crystals (PCs) are a category of optical resonators that hold promise for digital resolution biosensing and microscopy [13,14]. A PC is a periodic arrangement of dielectric permittivity which can produce many of the same phenomena for photons that the atomic potential produces for electrons [15]. By adjusting the parameters/materials of the PC, the electromagnetic fields associated with light can be manipulated to generate resonances at specific wavelengths for enhancement of light-matter interactions. Specifically, the resonances of a PC result in the formation of electromagnetic standing waves with intensities that are enhanced relative to the intensity of an illuminating light source, such as an LED or a laser. Recent research has shown that gold nanoparticles (AuNP) with localized surface plasmon resonances (LSPR) that spatially and spectrally overlap with the PC's surface-confined resonant electromagnetic field yield a 10-fold amplification of the absorption efficiency [16]. The synergistic coupling between the gold nanoparticle and the PC surface leads to the capability to observe individual gold nanoparticles using a conventional inverted optical microscope, as the enhanced NP absorption can attenuate light that is reflected into a microscope objective.

Utilizing PC-AuNP resonant coupling, a new form of biosensor microscopy called Photonic Resonator Absorption Microscopy (PRAM) was recently demonstrated [17–20]. The initial implementation of PRAM was a line-scanning microscopy, in which a line of normally incident LED illumination spans a ~400 µm width across the PC surface [17], and the resulting resonantly reflected light is directed into the entrance slit of an imaging spectrometer, enabling collection of resonant reflection spectra from 512 distinct locations along the illumination line. To generate a 2-dimensional image, the PC is translated in small increments under the illumination line to

Biomedical Optics EXPRESS

gather additional sets of spectra that represent the resonant reflection characteristics of an array of spatial locations across the PC surface area. While the line scanning PRAM instrument can analyze the resonant reflection spectra of each pixel for its peak intensity value (PIV), and can thus easily differentiate pixels with a surface-attached AuNP from the background [17], the instrument is well-suited only to a laboratory environment due to its requirement for a spectrometer and high precision computer-controlled motion stage.

Using the line-scanning PRAM instrument, a series of high sensitivity, rapid, and high dynamic range assay applications have been demonstrated for digital resolution detection of miRNA and protein target biomarkers, including detection from serum. Using an approach called "Activate Capture + Digital Counting" (AC + DC), resonant-matched AuNPs are functionalized with a probe molecule that selectively binds with a target biomarker molecule from the test sample. AuNPs are "activated" when they bind with the target, which renders them able to bind with a capturing molecule that is immobilized on the PC biosensor surface. In the context of an assay for a target protein molecule, a capture antibody is immobilized on the AuNP, and a secondary antibody is immobilized on the PC [20,21]. By mixing the test sample with the functionalized AuNPs in a liquid-containing well with the PC biosensor comprising the bottom surface, the AC + DC assay results in formation of a biomolecular complex on the PC surface in which each captured AuNP represents detection of one target biomarker molecule. AC + DC assays are single step, room temperature, digital resolution protocols that have yielded 100 aM limits of detection [19]. For example, an AC + DC assay to detect HIV-1 p24 antigen in human serum with a 35 min. workflow achieved a thousand-fold dynamic range (1–10^3 pg mL^{-1}) and a detection limit of 1 pg mL^{-1} [21].

Oligonucleotide based hybridization reactions have become an attractive strategy for biomolecule detection. The 'toehold probe' technology utilizes the thermodynamic hybridization of nucleic acids, which enables the detection of target sequences with single nucleotide precision [22]. In principle, toehold probes contain partially hybridized double-stranded nucleic acid sequences with an overhanging region (or toehold). This region can be tuned to undergo a competitive strand displacement reaction, where the target sequence anchors to the toehold, thereby forming a longer double-stranded sequence [23]. The AC + DC assay approach has also been applied using the line-scanning PRAM instrument for ultrasensitive and ultraselective detection of specific miRNA sequences [19], where nucleic acid toehold probes are applied to the AuNP, which, when a protector strand is displaced by the target miRNA, reveals a nucleic acid sequence that selectively recognizes a single strand DNA sequence immobilized on the PC surface. Our prior work demonstrated an AC + DC assay for miRNA-375 with 100 aM limits of detection, 5 logs dynamic range, and a very high degree of selectivity against non-target RNA sequences [19].

In this work, we demonstrate a PRAM instrument (Fig. 1(C)) that eliminates the spectrometer and the motion stage used in our previous reports. As shown schematically in Fig. 1, the main components of the instrument are a low intensity LED, a linear polarizing filter, a microscope objective, and a webcam-quality silicon CMOS image sensor. The LED illumination wavelength is selected to coincide with the PC resonant reflection wavelength, so that the highly efficient resonant reflection results in high intensity recorded on the pixels of the image sensor (Fig. 1(B)). The presence of a single AuNP, whose plasmon resonant wavelength has been strategically chosen to match the PC resonant wavelength, results in an easily measured reduction in the reflected intensity from the PC, which appears as a single dark spot (compared with the surrounding bright background) on the image sensor. The AC + DC assay, measured by the POC PRAM instrument, represents a digital biomolecular detection approach in which each captured nanoparticle represents one target biomolecule from the test sample. By the virtue of the synergistic plasmonic-photonic coupling, strongly localized electric field on the surface of the AuNP leads to good signal-to-noise ratio for each surface-captured particle, as validated through numerical simulation in Fig. 1(B). It is noteworthy that although surface-captured AuNP could

Biomedical Optics EXPRESS

also lead to PC resonant wavelength shift, the FWHM of the LED is large in comparison thus this secondary effect does not have great influence on the overall performance.

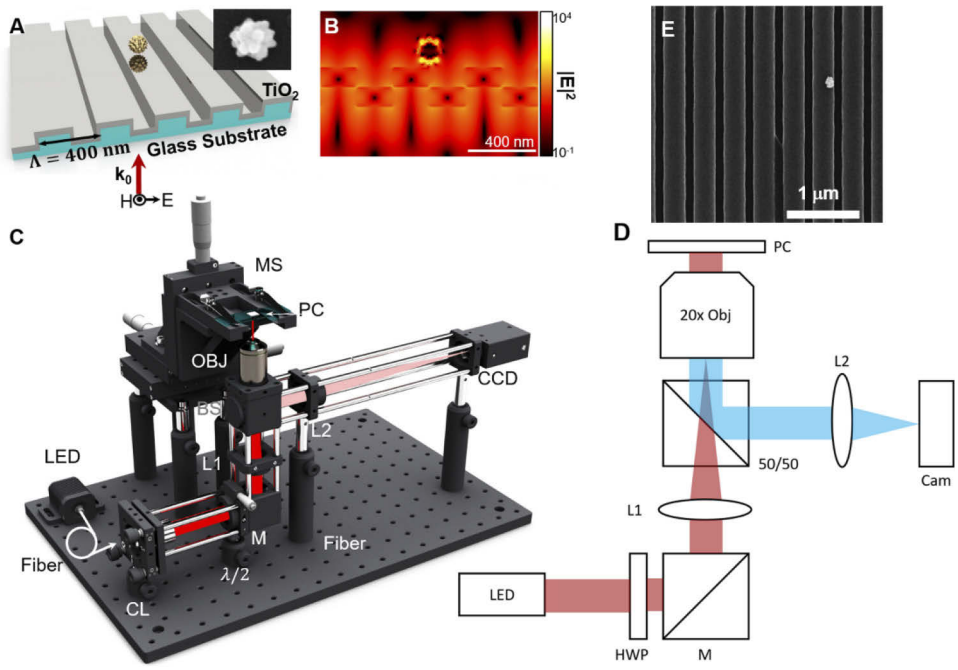

Fig. 1. (A) Schematic of the plasmonic gold nano-urchin (AuNU) nanoparticle on a photonic crystal (PC) surface. Inset: SEM image of a representative AuNU. (B) Electric field intensity distribution of the plasmonic-photonic hybrid at the resonant wavelength of the PC, where strong localized electric field can be observed near the tips of the AuNU, resulting in enhanced absorption efficiency when the LSPR of the AuNU matches the resonant wavelength of the PC. (C) Illustration of the POC PRAM instrument CL: collimator lens; λ/2: half wave plate; M: mirror; L: lens; BS: beam splitter; OBJ: objective; MS: motion stage. (D) Schematic drawing showing the parts of the POC PRAM. (E) SEM image of the PC.

2. Experimental

2.1. Design and principle of the compact photonic resonator absorption microscope

The PC structure used in our work has been described in previous reports [17–21]. Briefly, as shown in Fig. 1(A) and Fig. 1(E), the PC is a nanostructured surface comprised of a linear grating (Period 380 nm, depth 97 nm, duty cycle 65%) etched into a glass substrate, upon which a high refractive index thin film of TiO_2 (Thickness 98.5 nm, n = 2.44) is applied by sputtering. The PC period and grating depth are designed so that, when the PC surface is immersed in an aqueous media, the structure provides a high efficiency (85%) resonant reflection at a wavelength of 625 nm, with a full-width at half-maximum of $\Delta\lambda$=4.24 nm. The PCs used in this work were fabricated by a commercial vendor (Moxtek, Orem, UT) to our design specifications on 8-inch diameter glass substrates, upon which the PC grating structure was patterned by holographic lithography and etched by reactive ion etching. The TiO_2 high-index film was deposited by sputtering, to yield the transmission spectrum shown in Fig. S2. After wafer-scale fabrication of the PC structure, the wafer is diced into 10.16×12.7 mm^2 chips that are used for biosensing experiments. Silicone rubber gaskets comprised of six 30 μl compartments are fabricated from polydimethylsiloxane

Biomedical Optics EXPRESS

(PDMS) elastomer, and adhered to the PC chip to provide liquid confinement. At the PC resonant wavelength, a surface-confined electromagnetic standing wave is established with an evanescent field that extends into the water media that covers the PC surface.

For the nanoparticles used in this work, we selected commercially available AuNU nanoparticles (Cytodiagnostics, Ontario) with a diameter of 90 nm due to their spherical symmetry and their surface plasmon wavelength that overlaps with the PC resonant wavelength [24]. The AuNU's "spiky" outer surface morphology (shown in Fig. S1(A)) offers a further advantage of a high surface area onto which biomolecular probes can be attached via surface chemistry. The absorbance spectrum of the AuNUs demonstrating its peak at 625 nm are shown in Fig. S1 (B). As described in previous reports [16,25], the spectral and spatial overlap between the PC resonant mode and the AuNU LSPR mode results in formation of a synergistic hybrid structure, where the PC actively channels its energy into the plasmonic resonator, which subsequently dissipates into the surrounding medium. The synergistic coupling behavior results in a one-order-of-magnitude amplification greater absorption cross section than possible for a AuNU on an ordinary unpatterned surface [16], and the observation of locally reduced reflection efficiency of light from the PC surface (Fig. S2).

Based on this principle, our POC PRAM detection instrument is configured to visualize AuNU attachment events via reduced reflection intensity using an inexpensive silicon-based image sensor. A schematic of the system is shown in Fig. 1(D). Port 1 is coupled to a fiber-coupled 617nm LED (M617F2, Thorlabs, 10.2 mW, FWHM = 15 nm), whose distal end provides a point-like source to a lens group (F810SMA-635, Thorlabs, NA = 0.25, f = 35.41 mm) utilized to expand and collimate the output beam. The LED center wavelength and FWHM were selected to include the PC resonant wavelength. A zero-order half-wave plate (WPH10M-633, Thorlabs) rotates the polarization of the collimated beam in order to excite the TM resonance mode of the PC. A plano-convex lens 'L1' (LA1509-A-ML, Thorlabs) is then used to achieve Köhler-type illumination, allowing the PC surface to be illuminated by a collimated beam at normal incidence. A manual three-axis stage (PT3, Thorlabs) is used to secure the PC chip at the focal plane of the plan-fluorite 20× objective (NA = 0.5). The reflected light from the PC is collected by the same objective and redirected by a 50/50 non-polarizing beam-splitter (CCM1- BS013, Thorlabs). A doublet 'L2' (AC254-200-A-ML, Thorlabs) projects the image plane onto a charge coupled device (CCD) camera (GS3-U3-51S5M-C, Point Grey), with a resolution of 177 nm/pixel. The cost of the system components is $6907.67, and the assembled system occupies a 12" x 18" optical breadboard base. A detailed list of components along with their commercial source and prices is provided in Table S1.

2.2. Materials and methods

2.2.1. Simple detection of AuNUs without performing an assay

To investigate the operation of the instrument without performing an assay, we initially sought to apply a low-density population of AuNUs to a "bare" PC using gravity and nonspecific adsorption. The PC was prepared by cleaning via sonication in acetone, isopropanol (IPA) and milliQ water for 2 min. each, followed by drying under compressed nitrogen. The carboxyl-coated AuNUs supplied by the manufacturer were then diluted 5000 times using molecular grade water. 5 µl of the diluted AuNUs were dropcast on the surface of the PC and allowed to settle for 30 min., followed by imaging collection with the POC PRAM instrument.

2.2.2. Preparation of the PC surface for toehold probe miRNA assays

The PC was cleaned by sonicating in acetone, IPA and milliQ water, respectively, for 2 min. each. It was subsequently dried under compressed nitrogen followed by oxygen plasma treatment (200W) at 500 mTorr pressure for 10 min. using a Pico Plasma System (Diener electronic, Germany). 100 µl of (3-Glycidoxypropyl) trimethoxysilane (GLYMO, Sigma Aldrich) was then

Biomedical Optics EXPRESS

added to each plasma treated PC in a glove box vacuum chamber. The PC was then dried in a vacuum oven at 80 °C for 6–8 hours. The silanized PC was subsequently cleaned by sonicating with methanol, toluene and milliQ water, respectively, for 2 min. each followed by drying with nitrogen.

The silanized PC was functionalized by incubating 1 cm^2 of its surface area with the DNA solution overnight. The capture DNA solution was synthesized by redispersing 20 µl of amino-terminated PC capture oligo dispersion in 1× TE buffer into 180 µl of 1 × TE buffer (pH 9). After overnight incubation, the PC was rinsed by a gradual decrease of TE buffer concentration from 1× to 0.01×. Finally, the PC was stored at 4 °C for future use. Immediately before running the assay, the functionalized PC was incubated with SuperBlock (in TBS) blocking buffer (Thermo Fisher Scientific) for 45 min. followed by washing with 1 × TE buffer.

2.2.3. Gold nanourchin probe synthesis and annealing with protector DNA

Lyophilized maleimide functionalized 90 nm AuNUs were conjugated to the probe DNA (Probe DNA: AuNU = 50:1) using a conjugation kit (Cytodiagnostics, Burlington, Ontario). 50 µl of 100 µM probe DNA was reduced in 5mM dithiothreitol (Sigma Aldrich) mixed in 1 × TE buffer. The reduced DNA was extracted 4 times using ethyl acetate (Sigma Aldrich). The extracted probe was then diluted to 100 pM (24 µl) and redispersed in the reaction buffer (84 µl) provided with the kit. 90 µl of the probe – reaction buffer mixture was subsequently added to a vial containing lyophilized maleimide AuNUs followed by an incubation in a shaker for 1 hour at room temperature. 10 µl of the kit-provided quencher solution was added to the resulting mixture and incubated for 15 min. The AuNU-probe DNA mixture was then centrifuged for 30 min. at 300 g to separate the conjugated AuNUs using 100 µl of conjugation buffer (1 × TE + 12.5 mM $MgCl_2$ (Sigma Aldrich) + 0.025% TWEEN 20 (Sigma Aldrich)).

The conjugated AuNUs were then annealed at 80 °C for 2 min. and cooled 0.5 °C every 30 seconds until the final temperature reached 18 °C. This process facilitated the hybridization between the probe and the protector DNA strands.

2.2.4. Detection assay for miRNA-375

The assay was performed in the presence of the following components: 1. AuNU-probe DNA, 2. target miRNA-375, 3. protector DNA 4. PC functionalized with capture DNA, and 5. 1 x TE buffer. The assay is based on the principle reported by Canady et al. [19], illustrated in Fig. 2. To detect miRNA-375, a constant amount of AuNU-probe DNA annealed with protector DNA was mixed with a specific concentration of miRNA-375 in a PDMS well attached to the PC, so the PC biosensor forms the entire bottom surface of the well. The concentration of the target was varied between 1 fM to 10 pM. Subsequently, the image of a 339×212 μm^2 area of the well was captured using the POC PRAM. The PRAM image area represents 1% of the total bottom surface of the well, and thus a portion of surface-captured AuNUs will be outside the field of view and not recorded.

2.2.5. Image processing

Four sub-fields of view (sub-FOVs) of 60 µm x 52 µm were manually selected from within the image to avoid any observed large artifacts (e.g. dust particles trapped between the PC and the glass slide) that could potentially lead to inaccurate AuNU counting. The selection of sub-FOVs further reduces the total surface area of the PC from which AuNUs are recorded to 240×208 μm^2. Thus, our detection approach characterizes the area density of AuNUs rather than a true count of the total number of AuNUs. Our motivation for performing image processing algorithms upon sub-FOVs rather than the full image is further motivated by variations in illumination intensity and thus AuNU contrast from the center of the image to the edges. Illumination of the PC through the distal end of an optical fiber results in an approximately Gaussian intensity distribution. The

Biomedical Optics EXPRESS

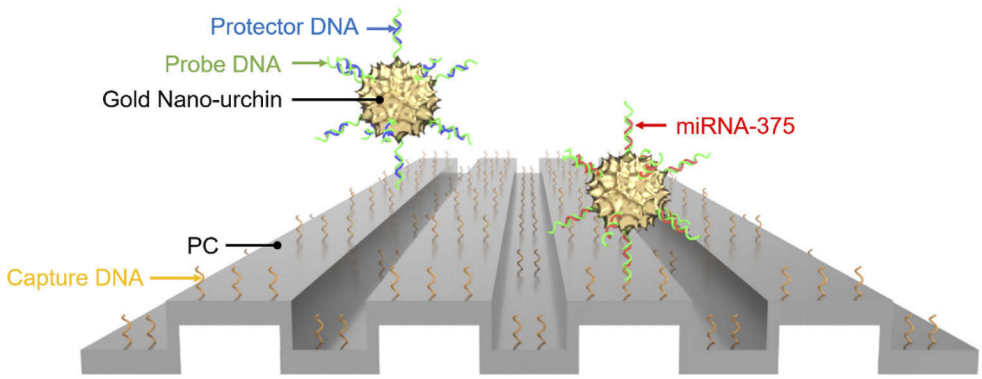

Fig. 2. Detection strategy for miRNA using engineered nucleic acid probes applied to the PC biosensor and the AuNU. The AuNU is prepared with a nucleic acid toehold probe, in which a protector strand of ssDNA is displaced by the target miRNA sequence, resulting in a new ssDNA sequence being revealed, after which the AuNU is said to be "activated." The newly revealed ssDNA base sequence is a complementary match to the capture ssDNA sequence on the PC biosensor surface. Activated AuNUs are subsequently captured, where each captured AuNU represents detection of one target miRNA molecule. The POC PRAM instrument is designed to digitally count captured AuNUs through the contrast they induce in the PC reflected intensity.

sub-FOV images were subjected to contrast enhancement using CLAHE. Adaptive thresholding followed by image binarization was applied to the contrast-enhanced images to obtain AuNU counts. AuNU numbers obtained from the four equally sized sub-FOV images are averaged to obtain a mean count. Mean counts calculated from independent replicate (N=3) PC biosensor wells for each experimental condition are subsequently divided by the sub-FOV area to obtain AuNU densities reported in units of counts/μm^2.

3. Results and discussion

3.1. Simple detection of AuNUs without performing an assay and image processing

Figure 3 shows the multistep process that is used to convert raw images from the CMOS sensor array into AuNP density values. Figure 3, Step 1 shows a representative PRAM image of surface-attached 90 nm AuNUs on the PC surface, gathered with the instrument. Four sub-FOV images of equal size (60 µm x 52 µm) are selected from the full image (Step 2). In this work, we used visual inspection to guide selection of the sub-FOV regions to intentionally avoid large artifacts (such as dust particles trapped between the PC and the glass slide) that could introduce errors in the automated image processing. At this point, the grey scale bar (minimum and maximum intensity) for each sub-FOV images is calculated. A 3D contour plot representing the distribution of AuNUs and their corresponding pixel intensities has been illustrated in Step 3, and such contour plots are generated by our software. The PC is a high efficiency resonant reflector for normally incident light in the 618–625 nm wavelength band, which falls inside the illumination bandwidth of the LED by design. Without the presence of AuNUs, the reflected pixel intensity will begin at a high baseline value, and be reduced by the local attachment of AuNUs. Due to the effects that include imperfect collimation, scattering, and diffraction, the measured intensity difference (ΔI) between a PC region without an AuNP (I_b) and a region with a single AuNP (I_{AuNP}), calculated by $\Delta I = I_b - I_{AuNP}$, is typically reduced by 12% - 40%, which is well above the shot noise limit of intensities recorded by the pixels of the image sensor. In Step 4, the intensity scale bar of the sub-FOV image is selected to encompass the background

Biomedical Optics EXPRESS

intensity and the reduced intensity of pixels that contain an AuNU. Next, we apply contrast enhancement to further differentiate pixels in the image with/without an AuNU. First, we apply the Contrast Limited Adaptive Histogram Equalization (CLAHE) function within Image J to the sub-FOV images. CLAHE computes histograms corresponding to distinct sections of the image, and uses the histograms to redistribute the pixel intensity (grayscale) values of the image. While ordinary AHE has a tendency to overamplify noise in relatively homogeneous regions of an image, CLAHE limits the extent of amplification, which is especially important for PRAM images with a sparse density of AuNUs. Due to variability in the illumination intensity across the image surface (due to the Gaussian distribution of light provided by the LED – which is brightest in the center, and least intense at the image edges) we observe that AuNU contrast is greatest in the image center. Although the introduction of beam homogenizer can provide a flat-top beam profile, in order to lower the overall costs and maintain the beam polarization, we utilized post-processing method to compensate this issue. In order to normalize the effects of non-equal illumination intensity, a second adaptive image thresholding algorithm is applied to the contrast enhanced sub-FOV images in Step 5. Here, each AuNP intensity is normalized against its local background intensity, which effectively classifies every pixel in the image into "AuNU" or "background." The final step of image processing is to derive a count of the AuNUs. In Step 6, the boundaries surrounding dark pixels in the contrast-enhanced image are obtained using the "bwboundaries" command in MATLAB. The size of each AuNU region is measured in terms of the number of pixels it occupies, which enables the particle counting to ignore any regions that are too large to be a single AuNU (for example, a dark region caused by a PC defect or dust particle) or any spurious dark pixels that are too small to represent a single AuNP. For visualization, the image of the boundaries is overlayed with the contrast-enhanced sub-FOV PRAM image, which is inspected visually to ensure that particles are not "missed" and that phantom boundaries are not being generated around regions with no nanoparticle. The "length" command in MATLAB is then used to calculate the number of boundary elements in the image, resulting in a nanoparticle count. Finally, the reported AuNU densities are calculated by averaging the AuNU numbers derived from all four sub-FOV images.

Representative images of 90 nm AuNUs attached to a PC surface obtained using our line-scanning PRAM instrument and the POC PRAM instrument are compared in Fig. 4(A-D). To prepare these images, AuNUs were dropcast upon the PC without performing an assay. For an area of 39×62 μm^2, the observed AuNU counts were 252 for the POC PRAM and 254 for the line-scanning PRAM. Therefore, the AuNU density for the POC PRAM were calculated to be 0.102 counts/μm^2, which is consistent with the AuNU density of 0.105 counts/ μm^2 obtained with the line scanning PRAM. Further area sub-selections from these images are shown in Fig. 4(E-F) to clearly depict the similarity in AuNU densities. We observed that at a specific time point and for the same area of the PC, the POC PRAM reported consistent AuNU densities with a coefficient of variability (CV) of approximately 0.003. In this case, time is an important parameter as we observed an increasing AuNU density as function of time.

3.2. Detection assay for miRNA-375

As a proof of principle, the POC PRAM instrument was used to measure an Activate Capture + Digital Counting (AC + DC) assay for miRNA-375. As summarized in Fig. 2, the AuNU is prepared with a nucleic acid toehold probe in which a protector strand is displaced by binding of the target miRNA to the probe. Displacement of the protector strand results in a newly-exposed ssDNA sequence to become available, and we refer to an AuNP with such a probe to be "activated." As the probe molecule is strategically designed for our purposes, we prepare the PC biosensor with an immobilized ssDNA sequence that is a complementary match to the newly exposed ssDNA sequence on the activated AuNU. Thus, when the activated AuNU reaches the PC surface by diffusion, it has the opportunity to be captured by Watson-Crick base pairing between the

Biomedical Optics EXPRESS

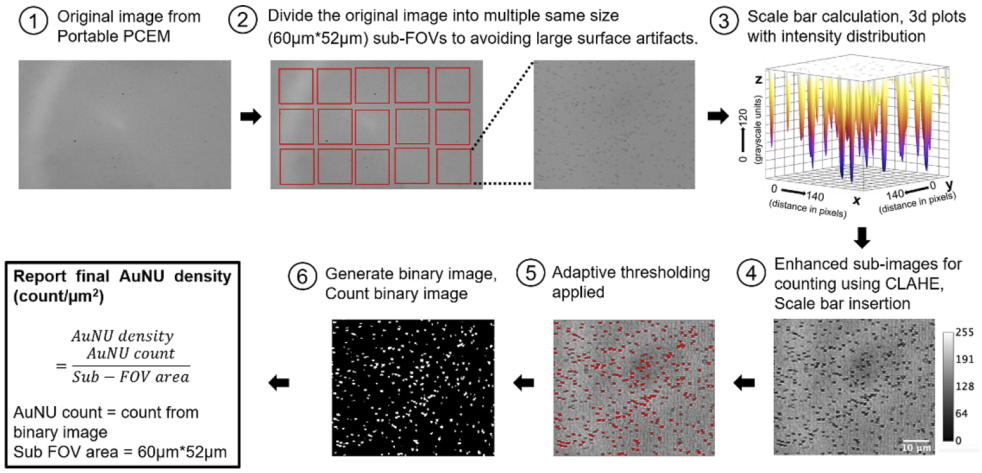

Fig. 3. Summary of steps used for processing images obtained from the POC PRAM instrument. Step1: Grey scale intensity images obtained from the image sensor chip, representing a 339×212 μm^2 region of the PC. Step 2: The full image is divided into a set of smaller field of view (FOV) images of 60×52 μm^2. Step 3: Scale bar and pixel intensity distribution plots are obtained. Each AuNU results in a 12 - 40% reduction in reflected intensity. Step 4: The sub-FOV images are contrast enhanced using CLAHE. Step 5: The enhanced images are subjected to Adaptive thresholding to generate a binary image. Step 6: The binary image is used for AuNU counting. The AuNU counts obtained from independent (N=3) experiments are divided by the sub-FOV area to obtain the final reported AuNU density (counts/μm^2).

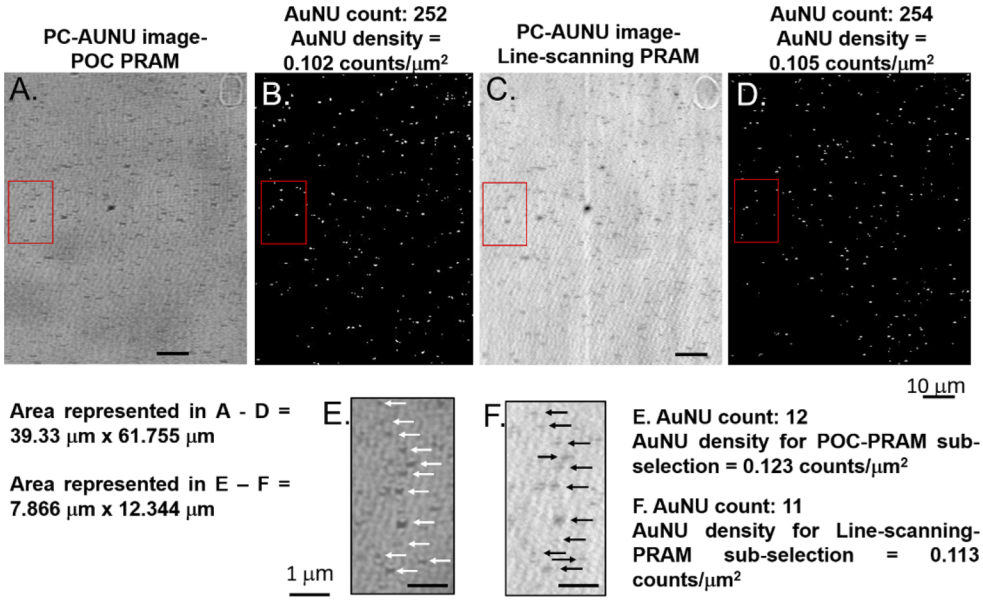

Fig. 4. Quantification of AuNU counts and densities as observed on the same region of the PC in the POC PRAM and the line-scanning PRAM instrument. Area sub-selections (indicated by the red box outline) in (A-F) have been further analyzed to indicate the AuNUs using white arrows for (E) and black arrows for (F).

Biomedical Optics EXPRESS

two ssDNAs. In this way, one target miRNA molecule in the test sample has the opportunity to activate one AuNU, which is subsequently captured and digitally counted with the PRAM instrument after sufficient incubation time. The assay is performed in a single step at room temperature, in which the test sample and probe-prepared AuNU solution is mixed in a well, in which the PC comprises the bottom surface. As discussed in [19], we provide an excess concentration of AuNUs, so that in solution the target molecules and AuNUs combine rapidly and the capture of activated AuNUs is limited by their rate of diffusion to the PC surface. To explore the kinetics of the activated AuNU capture, PRAM images were obtained after 10 min., 30 min., and 60 min. of incubation.

Figure 5(A) shows a matrix of sub-FOV images of AuNU binding to the PC at three time points (10, 30, 60 min.) for concentrations of the target miRNA- 375 spiked into 1 x TE buffer ranging between 1 fM to 10 pM. The PRAM images (incorporating information from all the sub-FOVs) were processed using our AuNU counting approach to yield the dose-response plots shown in Fig. 5(B-D), in which we observe dose-dependent AuNU densities over 5 logs of dynamic range. Each concentration was measured in N=3 independent wells with independent PC biosensors to yield the error bars, representing one standard deviation for each point. An increase in the number of AuNUs over concentration and time was attributed to the coupled kinetic dependence of the toehold strand-displacement reaction and the surface capture of the activated AuNU-probe DNA on the miRNA-375 concentration [19]. As a negative experimental control, non-specific deposition of AuNUs was recorded when no target miRNA-375 was added to the reaction, but the probe DNA-AuNUs were present. Fig. S3 (A-F) summarizes the variation of AuNU densities

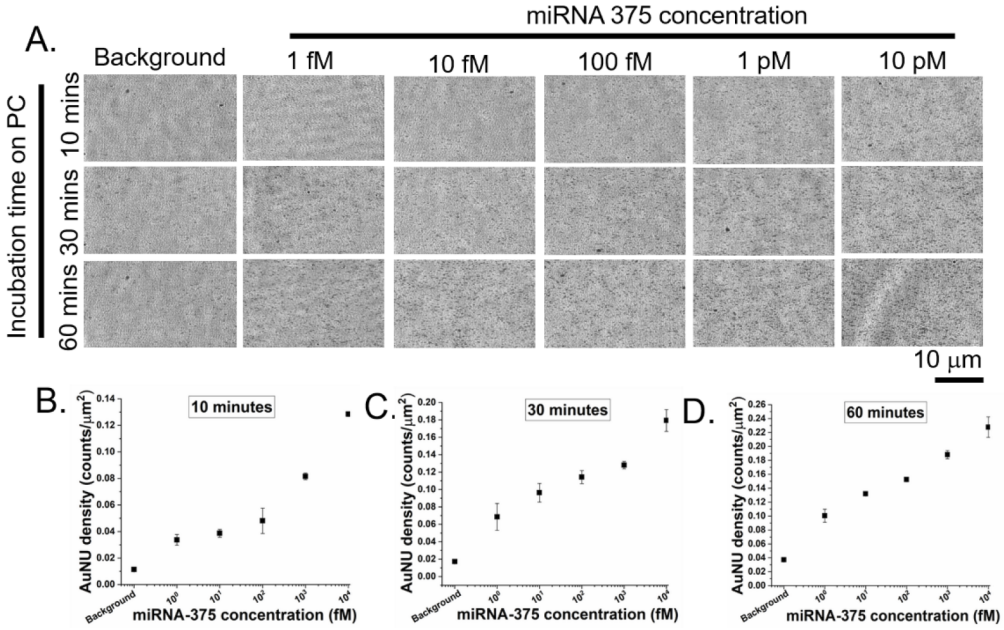

Fig. 5. Results of an AC + DC assay for miRNA-375 measured with the POC PRAM instrument. (A) Selected representative images of sub-FOVs for AuNP binding to the PC surface as a function of miRNA-375 concentration (1 fM-10 pM) taken at several time points (10, 30, 60 min.) during the assay incubation time. Dose-response plots of AuNP density as a function of miRNA-375 concentration recorded at (B) 10 min., (C) 30 min. and (D) 60 min. of incubation time. Error bars represent standard deviation of N=3 independent assay wells for each concentration. The negative experimental control ("Background") is the sample, which has the AuNU-probe DNA but no target miRNA-375.

Biomedical Optics EXPRESS

as a function of time for target concentrations ranging between 0 fM – 10 pM. It is interesting to note that a linear behavior is primarily observed in curves B-F, which indicates a possibility of further binding between the target, AuNU-probe DNA and capture DNA. As shown in Fig. 5(A), for the wells labeled as "Background" non-specific capture and counting of AuNU was very low. AuNU density values ranging between 0.011 counts/μm^2 – 0.037 counts/μm^2 for 10–60 min. were observed. The non-specific deposition of AuNUs was attributed to the direct hybridization between unprotected probe DNA and the capture oligo [19,26]. Initially, it was observed that the AuNU-PC surface reached saturation after approximately 60 min. of incubation. Hence, we subsequently tested the binding capacity of the AuNU-probe DNA with miRNA-375 by serially diluting the target concentrations between 1fM – 10 pM within 60 min. and reported AuNU densities. Based on the dose- response curve in Fig. 5, the limit of detection was calculated to be 276 aM for a 60-min. incubation time. The limit of detection for a 30-min. incubation time was 160 aM and the detection limit after 10 min. of incubation time was 303 aM. An important aspect of this assay is PC surface blocking. We observed that in the absence of blocking buffer, the AuNU-PC surface was saturated within 10 min. With an increased blocking time, we observed an increase in the saturation time to 60 min. along with a decrease in non-specific AuNU deposition. These observations and results are consistent with the detection limits obtained for performing the same assay measured with the line-scanning PRAM instrument, in which a 100 aM detection limit was achieved with a 120-min. incubation time.

3.3. Specificity testing for single-mismatch miR-375 discrimination

The selectivity was tested by using two different single-base mismatch variants to our target miRNA-375 denoted by MMx, where x represents the nucleotide mismatch position starting from the 5' end. Figure 6 demonstrates that both the mismatch variations (1st nucleotide and 5th nucleotide) resulted in a significant decrease in the AuNU density on the PC. The concentration of both the MM sequences and perfectly matched (PM) sequence was 10 pM. AuNU densities were observed to increase as a function of time (Fig. 6). At 60 min., an average AuNU density observed for 10 pM MM_1 was 0.022 counts/μm^2 and for 10 pM MM_5 was 0.046 counts/μm^2. As seen in Fig. 6, the PM sequence demonstrated almost 10 times higher AuNU densities compared to that of MM_1 and about 5 times higher than MM_5.

Biomedical Optics EXPRESS

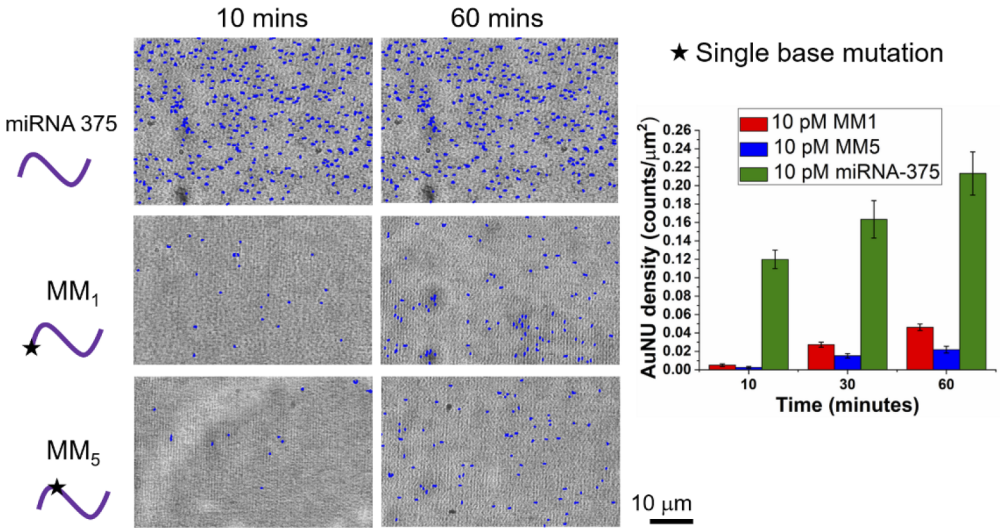

Fig. 6. Demonstration of selectivity for the AC + DC assay. AuNUs binding to the PC surface in the presence of 10 pM perfect match target (miRNA-375) and single mismatch variants inserted at the 1st nucleotide (MM_1) and the 5th nucleotide (MM_5) at 10 pM concentrations. Reported AuNU counts for all the three variants measured by the POC PRAM at 10, 30 and 60 min. of the assay incubation time.

4. Conclusion

This paper demonstrates a POC version of the PRAM instrument which eliminates the need for spectroscopic measurement of the PC resonant reflection spectra on a pixel-by-pixel basis. Further, the POC PRAM instrument captures an image of a large field of view in a single image acquisition, rather than through a line-scanning process that requires a precision computer-controlled motion stage. By eliminating the need for some of the most expensive components of the line-scanning PRAM instrument, the resulting POC PRAM instrument achieves a small form factor suitable for desktop environments, with a cost of components ($7,000 to assemble one instrument using parts purchased from catalogs) that is compatible with widespread adoption in clinics and diagnostic laboratories. With further efforts in engineering design for manufacturing and efficiencies from scaling, we expect that the cost of a product based on this design can be reduced further. The main components of the instrument are a conventional red LED, a microscope objective, a polarizing filter, and a webcam-quality CMOS image sensor.

Current point-of-care biosensing approaches often utilize fluorescence-based methods due to their high sensitivity in comparison to label-free detection, despite the potential for fluorescent tags to alter the functional properties through epitope blocking or conformational change that can modify binding affinity and isothermal equilibrium of the labeled molecule [27]. Importantly, fluorescent labels suffer from issues that include photobleaching and highly variable quantum efficiency, which complicates derivation of quantitatively accurate counting of target molecules. Further, the low emission intensity from fluorescent tags leads to the requirement for high intensity illumination sources and expensive high-sensitivity image sensors that must incorporate cooling and electron multiplication technology to observe individual tags using high numerical aperture oil-immersion objectives. Because PRAM does not utilize fluorescent labels, it is not subject to photobleaching effects, enabling gathering of long-term kinetic data without loss of signal. Additionally, PRAM utilizes a low-cost, low intensity LED illumination source, a web-cam quality CMOS image sensor, and low numerical aperture air-media objectives to observe

Biomedical Optics EXPRESS

a large sensor field of view. Each AuNP tag provides a sufficiently high signal-to-noise ratio to enable digital resolution counting of tagged biomolecular targets with a compact and inexpensive instrument.

Despite removal of the ability to observe the detailed resonant reflection spectra from each pixel in a PRAM image, the POC PRAM instrument is nonetheless capable of accurately counting surface-attached AuNUs, with high contrast achieved when the AuNUs are strategically selected so that their LSPR absorption wavelength matches the PC resonant reflection wavelength. As the AuNU density is the measured variable of the assay, it is only necessary to observe individually captured AuNUs with sufficient reduction of reflected intensity from the bright reflected background intensity. Here, we applied conventional image processing algorithms to discriminate darker regions of the reflected image from the brighter surrounding background to separate "in particle" from "not a particle" discrete digital bins, and to further apply a common algorithm to count the dark regions. We note that it is not our intention here to enumerate the miRNA molecules in the test sample, but rather to measure dose-dependent changes in AuNU density that enable estimation of the target molecule concentration. We have shown that AuNP densities measured with the POC PRAM instrument yield very similar detection limit, dynamic range, selectivity, and dose-dependent AuNU density as the line-scanning PRAM instrument.

A further capability afforded by the POC PRAM instrument is the ability to capture images from a large field of view very rapidly. A single image acquisition requires only 6.1 msec of integration time to measure the reflected intensity of a $339 \times 212\ \mu m^2$ PC area. Therefore, it is not difficult to acquire multiple images of the same region at different time points to measure kinetic properties of detection processes. In this work, we simply imaged the PC at 10, 30, and 60 min. increments to observe the relatively slow process of diffusion responsible for gathering activated AuNUs to the PC surface for capture. However, we can also envision taking series of images at much shorter intervals to observe dynamic association/dissociation processes, and to measure the intrinsic properties of biomolecular interactions at the level of single units, using AuNPs as the tag that is captured or removed when an immobilized probe interacts with an immobilized molecule on the PC biosensor surface. Alternatively, the ability to easily capture many images can be used to spatially scan a PC surface to record interactions taking place in separate "active" and "reference" regions, or to record multiplexed tests taking place in separate wells. While we utilized macro-scale wells in this work, we can envision applying our approach to quantifying biomolecular interactions taking place within many parallel microfluidic compartments or flow channels.

Funding. National Institutes of Health (R01 EB029805, R01 CA227699-01); Jump ARCHES endowment through the Health Care Engineering Systems Center; Zhejiang University ZJU-UIUC Joint Research Center (DREMES202001); Ronald H. Filler Scholarship for Cancer Scholars; Illinois Scholars in Undergraduate Research (ISUR) Scholarship.

Acknowledgments. All research was conducted in the Micro and Nanotechnology Laboratory. The authors would like to enthusiastically thank all the members of the Nanosensors Group (NSG) and staff in the Nick Holonyak Jr. Micro and Nanotechnology Laboratory for their support.

Disclosures. The authors declare no conflicts of interest.

Data availability. Data underlying the results presented in this paper are not publicly available at this time but may be obtained from the authors upon reasonable request.

Supplemental document. See Supplement 1 for supporting content.

References

1. F. Yesilkoy, R. A. Terborg, J. Pello, A. A. Belushkin, Y. Jahani, V. Pruneri, and H. Altug, "Phase-sensitive plasmonic biosensor using a portable and large field-of-view interferometric microarray imager," Light: Sci. Appl. **7**(2), 17152 (2018).
2. Z. Yin, H. Guo, Y. Li, J. Chiu, and L. Tian, "Ultrastable plasmonic bioink for printable point-of-care biosensors," ACS Appl. Mater. Interfaces **12**(32), 35977–35985 (2020).

Biomedical Optics EXPRESS

3. S. K. Elledge, X. X. Zhou, J. R. Byrnes, A. J. Martinko, I. Lui, K. Pance, S. A. Lim, J. E. Glasgow, A. A. Glasgow, and K. Turcios, "Engineering luminescent biosensors for point-of-care SARS-CoV-2 antibody detection," Nat. Biotechnol. 1–8 (2021).
4. X. Cao, Y. Ye, and S. Liu, "Gold nanoparticle-based signal amplification for biosensing," Anal. Biochem. **417**(1), 1–16 (2011).
5. A. Belushkin, F. Yesilkoy, and H. Altug, "Nanoparticle-enhanced plasmonic biosensor for digital biomarker detection in a microarray," ACS Nano **12**(5), 4453–4461 (2018).
6. M. Dubrovsky, M. Blevins, S. V Boriskina, and D. Vermeulen, "High contrast cleavage detection," Opt. Lett. **46**(11), 2593–2596 (2021).
7. A. J. Haes, S. Zou, G. C. Schatz, and R. P. Van Duyne, "A nanoscale optical biosensor: the long range distance dependence of the localized surface plasmon resonance of noble metal nanoparticles," J. Phys. Chem. B **108**(1), 109–116 (2004).
8. O. Avci, N. L. Ünlü, A. Y. Özkumur, and M. S. Ünlü, "Interferometric reflectance imaging sensor (IRIS)—a platform technology for multiplexed diagnostics and digital detection," Sensors **15**(7), 17649–17665 (2015).
9. J. Ortega-Arroyo and P. Kukura, "Interferometric scattering microscopy (iSCAT): new frontiers in ultrafast and ultrasensitive optical microscopy," Phys. Chem. Chem. Phys. **14**(45), 15625–15636 (2012).
10. J. O. Arroyo, D. Cole, and P. Kukura, "Interferometric scattering microscopy and its combination with single-molecule fluorescence imaging," Nat. Protoc. **11**(4), 617–633 (2016).
11. R. W. Taylor and V. Sandoghdar, "Interferometric scattering (iSCAT) microscopy and related techniques," in *Label-Free Super-Resolution Microscopy* (Springer, 2019), pp. 25–65.
12. G. Young and P. Kukura, "Interferometric scattering microscopy," Annu. Rev. Phys. Chem. **70**(1), 301–322 (2019).
13. S. Jahns, M. Bräu, B.-O. Meyer, T. Karrock, S. B. Gutekunst, L. Blohm, C. Selhuber-Unkel, R. Buhmann, Y. Nazirizadeh, and M. Gerken, "Handheld imaging photonic crystal biosensor for multiplexed, label-free protein detection," Biomed. Opt. Express **6**(10), 3724–3736 (2015).
14. Y. Zhang, Y. Zhao, and R. Lv, "A review for optical sensors based on photonic crystal cavities," Sens. Actuators, A **233**, 374–389 (2015).
15. J. D. Joannopoulos, R. D. Meade, and J. N. Winn, *Photonic Crystals: Molding Flow of Light* (MIT Press, 1995).
16. Q. Huang and B. T. Cunningham, "Microcavity-mediated spectrally tunable amplification of absorption in plasmonic nanoantennas," Nano Lett. **19**(8), 5297–5303 (2019).
17. Y. Zhuo, H. Hu, W. Chen, M. Lu, L. Tian, H. Yu, K. D. Long, E. Chow, W. P. King, and S. Singamaneni, "Single nanoparticle detection using photonic crystal enhanced microscopy," Analyst **139**(5), 1007–1015 (2014).
18. W. Chen, K. D. Long, M. Lu, V. Chaudhery, H. Yu, J. S. Choi, J. Polans, Y. Zhuo, B. A. C. Harley, and B. T. Cunningham, "Photonic crystal enhanced microscopy for imaging of live cell adhesion," Analyst **138**(20), 5886–5894 (2013).
19. T. D. Canady, N. Li, L. D. Smith, Y. Lu, M. Kohli, A. M. Smith, and B. T. Cunningham, "Digital-resolution detection of microRNA with single-base selectivity by photonic resonator absorption microscopy," Proc. Natl. Acad. Sci. **116**(39), 19362–19367 (2019).
20. B. Zhao, C. Che, W. Wang, N. Li, and B. T. Cunningham, "Single-step, wash-free digital immunoassay for rapid quantitative analysis of serological antibody against SARS-CoV-2 by photonic resonator absorption microscopy," Talanta **225**, 122004 (2021).
21. C. Che, N. Li, K. D. Long, M. Á. Aguirre, T. D. Canady, Q. Huang, U. Demirci, and B. T. Cunningham, "Activate capture and digital counting (AC+ DC) assay for protein biomarker detection integrated with a self-powered microfluidic cartridge," Lab Chip **19**(23), 3943–3953 (2019).
22. D. Y. Zhang and E. Winfree, "Control of DNA strand displacement kinetics using toehold exchange," J. Am. Chem. Soc. **131**(47), 17303–17314 (2009).
23. X. Zhuang, H. L. L. Yu, and I.-M. Hsing, "Toehold probe-based interrogation for haplotype phasing of long nucleic acid strands," Anal. Methods **12**(34), 4185–4190 (2020).
24. Cytodiagnostics, "Maleimide Gold NanoUrchin," https://portal.cytodocs.com/documents/Product-Sheets/Product-Sheet-Maleimide-Activated-Gold-NanoUrchins.pdf.
25. J.-N. Liu, Q. Huang, K.-K. Liu, S. Singamaneni, and B. T. Cunningham, "Nanoantenna–microcavity hybrids with highly cooperative plasmonic–photonic coupling," Nano Lett. **17**(12), 7569–7577 (2017).
26. A. Johnson-Buck, J. Li, M. Tewari, and N. G. Walter, "A guide to nucleic acid detection by single-molecule kinetic fingerprinting," Methods **153**, 3–12 (2019).
27. Y.-S. Sun, "Use of microarrays as a high-throughput platform for label-free biosensing," J. Lab. Autom. **20**(4), 334–353 (2015).